

# Atmospheric Circulation and Composition of GJ1214b

Kristen Menou<sup>1</sup>

## ABSTRACT

The exoplanet GJ1214b presents an interesting example of compositional degeneracy for low-mass planets. Its atmosphere may be composed of water, super-solar or solar metallicity material. We present atmospheric circulation models of GJ1214b for these three compositions, with explicit grey radiative transfer and an optional treatment of MHD bottom drag. All models develop strong, superrotating zonal winds ( $\sim 1\text{-}2$  km/s). The degree of eastward heat advection, which can be inferred from secondary eclipse and thermal phase curve measurements, varies greatly between the models. These differences are understood as resulting from variations in the radiative times at the thermal photosphere, caused by separate molecular weight and opacity effects. Our GJ1214b models illustrate how atmospheric circulation can be used as a probe of composition for similar tidally-locked exoplanets in the mini-Neptune/waterworld class.

## 1. Introduction

The exoplanet GJ1214b has a mass of  $6.5M_{\oplus}$  and a radius of  $2.65R_{\oplus}$  (Charbonneau et al. 2009). This mass-radius combination does not permit a unique inference of the bulk composition of the planet, because of significant compositional degeneracies in the structural models (e.g. Fortney et al. 2007; Adams et al. 2008). Possibilities include a substantial envelope of water or hydrogen-dominated gas (perhaps enriched in heavy elements), above a massive solid/icy core (Rogers & Seager 2010; Nettelmann et al. 2011). We refer to such low mass exoplanets with deep envelopes of H or H<sub>2</sub>O as mini-Neptunes/waterworlds.

In a compositionally degenerate situation like that of GJ1214b, a promising method to constrain the atmospheric composition is to obtain a transmission spectrum of the planet as it transits its parent star. Indeed, the depth of atmospheric absorption features during transit is a direct measure of the atmosphere's mean molecular weight (Miller-Ricci et al. 2009; Miller-Ricci & Fortney 2010). Recently, such measurements have been performed for GJ1214b by several groups, at different wavelengths. Several reported transit spectra

---

<sup>1</sup>Department of Astronomy, Columbia University, 550 West 120th Street, New York, NY 10027

suggest a significantly metal-enriched or water atmosphere for GJ1214b (Bean et al. 2010, 2011; Desert et al. 2011; Crossfield et al. 2011), with one conflicting suggestion of a metal-poor atmospheric composition (Croll et al. 2011).

Here, we propose a complimentary probe of atmospheric composition for tidally-locked mini-Neptunes/waterworlds based on their specific regime of atmospheric circulation. Using GJ1214b as an example, we show that variations in atmospheric mean-molecular weight and opacities can have a strong enough effect on the degree of eastward heat advection at the thermal photosphere that secondary eclipses and thermal phase curves may also be used to consolidate our knowledge of the atmospheric composition of these planets. In §2, we describe our setup for modeling atmospheric circulation on GJ1214b, using three different compositions. Our model results and their interpretation are presented in §3, before we conclude in §4.

## 2. Models

To model the atmospheric circulation of GJ1214b, we use the Intermediate General Circulation Model (IGCM; Hoskins & Simmons 1975). It is a well-tested and accurate solver of the primitive equations of meteorology, which are satisfied by a shallow atmosphere of ideal gas in hydrostatic balance on a rotating planet. We use IGCM version 3, which contains several major improvements over earlier versions (Forster et al. 2000). The pseudo-spectral, semi-implicit dynamical component is described and tested in Menou & Rauscher (2009). Our implementation of IGCM3 for the study of gaseous exoplanets is described in Rauscher & Menou (2011b).

We assume that GJ1214b has a circular orbit and that the planet’s rotation is tidally synchronized with its orbit.<sup>1</sup> This leads to steady hemispheric forcing of the permanently irradiated dayside, with a substellar flux of  $2.15 \times 10^4 \text{ W m}^{-2}$  for GJ1214b. The two-stream radiative transfer scheme employed, which was adapted from the non-grey version of Forster et al. (2000), treats separately the shortwave (stellar) and longwave (thermal) radiation, with two different grey opacities. It is the same scheme as the one extensively tested in Rauscher & Menou (2011b), except that we do not implement a switch to the diffusion approximation in the model deepest layers here.

For numerical stability and to model small-scale dissipation (e.g., Thrastarson & Cho 2011), hyperdissipation is included. It acts upon the vertical component of the flow relative

---

<sup>1</sup>We refer to the rotational (and orbital) period of the planet as a planet day ( $\simeq 1.58$  Earth days).

vorticity, the flow divergence, and the temperature fields with an iterated Laplacian of order 8 and a hyperdissipation coefficient  $\nu_{\text{diss}} = 6.9 \times 10^{43} \text{ m}^8 \text{ s}^{-1}$  chosen so that the smallest resolved structures are diffused in 0.25 planet day.

A dry convective adjustment scheme is used to mix entropy at each timestep in all the atmospheric columns found to be convectively unstable. In practice, given the stably-stratified nature of the vertical profiles emerging in our models, convective adjustment is typically used only early in the runs, when the flow adjusts to the radiative forcing from the prescribed initial conditions. The atmosphere is started at rest. The initial temperature field is set as quasi-isothermal at  $T = 920 \text{ K}$  and subjected to spatially uniform 1D-averaged irradiation for 0.5 planet days before the hemispheric forcing is imposed. (Other comparable temperature initial conditions yield similar model results.) To break initial symmetry, we also include noise in the form of small amplitude random perturbations in the surface pressure field.

**Numerical Resolution and Convergence** – All six models presented here were run at T31L30 resolution, which corresponds to slightly less than  $4^\circ$  in latitude and longitude, with 30 logarithmically spaced vertical levels. The vertical domain extends from 0.1 mbar to 10 bar, so that our bottom boundary is above the radiative-convective boundary at  $\gtrsim 10$  bar for the compositions of interest (Miller-Ricci & Fortney 2010). We also ran  $\sim 50$  additional models at lower resolutions (T10L20 and T21L20) to evaluate numerical convergence and to survey the parameter space of circulations on GJ1214b, with variations in opacities, mean molecular weight, intrinsic heat flux (up to 1% of the irradiation flux) and bottom drag. These lower resolution results are generally consistent with the higher resolution versions presented in Figs 1-4, with minor quantitative differences.

**Composition, Opacities and Mean Molecular Weights** – The composition of the atmosphere of GJ1214b is presently unknown. Possibilities include a composition that is H-dominated, with solar or super-solar composition,  $\text{CO}_2$ -dominated or  $\text{H}_2\text{O}$ -dominated (Rogers & Seager 2010). Since our main interest here is to explore the interplay between atmospheric circulation and composition, we choose to focus on three particular compositions: water,  $\times 30$  supersolar and solar composition. These three compositions allow us to separate rather well the effects of molecular weight and opacity variations on the atmospheric circulation regime, as described below. For convenience, we refer to models with such compositions as Water, Supersol and Solar.

The 1D radiative-convective models of GJ1214b by Miller-Ricci & Fortney (2010) show that temperature-pressure profiles, and therefore opacities, are quite similar for a water and a  $\times 30$  supersolar composition. From the point of view of atmospheric circulation, different behaviors between such atmospheres will thus be mostly caused by differences in mean

molecular weight. By contrast, the Solar model has a molecular weight only moderately smaller than that of the Supersol model, but substantially weaker opacities. Therefore, our choice of three compositions emphasizes differences in mean molecular weights (Water vs. Supersol) and in opacities (Supersol vs. Solar). Using mean molecular weights  $\mu \simeq 18, 3.3$  and 2.2 for the Water, Supersol and Solar models, we deduce the gas constant values listed as  $\mathcal{R}$  in Table 1. We assume the same value of  $\kappa = \mathcal{R}/C_p$  in all models, where  $C_p$  is the specific heat at constant pressure (see Table 1).

We choose the grey opacity coefficients in our models so as to match as closely as possible the temperature-pressure profiles of Miller-Ricci & Fortney (2010) for the Water, Supersol ( $\times 30$ ) and Solar compositions, using the simple grey radiative solutions of Guillot (2010) as a comparison tool.<sup>2</sup> We find reasonable matches for the values of the visible and thermal opacity coefficients listed in Table 1. We pay close attention to the location of the shortwave and longwave photospheres, indicated by turning points in the profiles, using the same dayside-averaging as Miller-Ricci & Fortney (2010). We neglect the planet’s intrinsic heat flux, which does not have a major impact at the atmospheric levels of interest. While our matches with such a grey model can only be approximate, we do not expect minor discrepancies in temperature-pressure profiles to affect our main conclusions. Indeed, our results largely rely on the simple effect that strong molecular weight and opacity variations have on the radiative times at the thermal photosphere (see §3).

**MHD Bottom Drag** – An outstanding question for the modeling of atmospheric circulation on planets with deep atmospheres is the nature of drag mechanisms limiting the atmospheric wind speeds. A promising mechanism for hot Jupiters with radiative equilibrium temperatures  $T_{\text{eq}} \gtrsim 1000$  K is the magnetic drag that results from induction by weakly-ionized zonal winds flowing through the poloidal planetary magnetic field (Perna et al. 2010; Rauscher & Menou 2011a,b; Menou 2011). A related mechanism has been proposed to limit wind speeds in the deep layers of the atmospheres of Solar System giant planets, from interactions with the interior adiabat in presumed solid-body rotation (Schneider & Liu 2009; see also Liu et al. 2008). Altogether, these arguments suggest that MHD drag may also be acting in the deep layers of the atmosphere of GJ1214b, possibly in the vicinity of the radiative-convective boundary, where atmospheric temperatures quickly rise above 1000 K (Miller-Ricci & Fortney 2010).

In the absence of a detailed drag model, we include MHD bottom drag in some of our models by applying linear Rayleigh drag in the two deepest layers. We adopt drag times

---

<sup>2</sup>Our two-stream radiative scheme has been successfully benchmarked against Guillot’s solutions (Rauscher & Menou 2011b).

of 40 and 20 planet days for the second-to-deepest and deepest model layers, respectively. This may be interpreted as including a weak boundary layer in our models, to represent interaction with the convective interior maintained in near solid-body rotation by the effects of MHD rigidity (Liu et al. 2008). Given the close proximity of our deepest model layers to the radiative-convective boundary, we do not include any latitudinal dependence of the drag, as may be geometrically more appropriate for Solar System gaseous giant planets with MHD coupling only at significant depth below the atmosphere (Schneider & Liu 2009).

We have verified that our main results do not depend on specifics of the MHD bottom drag treatment (one- vs. two-layer drag, stronger vs. weaker drag), although some detailed aspects of the circulation regime can (see §3). This robustness is illustrated in Fig. 4, where models with and without bottom drag show consistent results. Table 1 lists the values of all the other important physical parameters adopted in our models of GJ1214b. To summarize, all six models are identical except for different values of the gas constant (mean molecular weight) and the opacity coefficients, with and without bottom drag.

### 3. Results

All model results are shown after long numerical integration of 5000 planet days (= 7800 Earth days). We find that steady-state is established well earlier than this for all the quantities shown in Figs 1-4. Spin-up is typically achieved after a few thousand planet days for the deepest model layers.

Figure 1 shows temperature-pressure<sup>3</sup> profiles in the Water model with bottom drag, for six different columns around the planet. Similar profiles are obtained in the Supersol model, with identical opacities. The profiles in the Solar model have broadly similar shapes but they are systematically shifted down in pressure, as a result of reduced opacities (see also Fig. 1 of Miller-Ricci & Fortney 2010 for such a shift). In all models, the poles are significantly colder than the equator. This feature, which can be attributed to limited meridional heat transport relative to the zonal transport, is also clearly apparent in the thermal flux maps (Fig. 3).

Figure 2 shows contour plots of the zonal average of the zonal wind velocity for the three models with drag, as a function of latitude and pressure in the atmosphere. A broad

---

<sup>3</sup>We use pressure as the vertical coordinate in our figures, rather than the model coordinate system,  $\sigma = p/p_s$ , because horizontal variations in surface pressures,  $p_s$ , are small enough in the models that the distinction between  $p$  and  $\sigma$  is unimportant.

superrotating equatorial jet with velocities  $\sim 1\text{-}2 \text{ km s}^{-1}$  is a common feature of all three models. Winds are also eastward (positive) almost everywhere in these deep atmospheres, with noticeably stronger winds at high latitude in the Supersol model, and particularly the Solar model. Westward (negative) winds are weak and only present in the deepest layers, where bottom drag is applied.

Our results are consistent with the theory of Showman & Polvani (2011), which points to the formation of superrotating equatorial jets under a broad range of atmospheric conditions for tidally-locked planets subject to dayside hemispheric forcing.<sup>4</sup> We estimate similar Rossby numbers,  $\text{Ro} \sim 1.5$ , and scaled Rhines lengths,  $L_\beta/R_p \sim 3.5$ , in all our models, for a  $1 \text{ km s}^{-1}$  wind scale (see Showman et al. 2010 for a review of basic atmospheric scales). By contrast, the scaled Rossby deformation radius is  $L_D/R_p \sim 0.7$  in the Water model,  $\sim 1.5$  in the Supersol model and  $\sim 1.8$  in the Solar model. Larger Rossby deformation radii in the Supersol and Solar models may be responsible for their broader patterns of eastward zonal winds, as seen in Fig. 2 (see also Showman & Polvani 2011).

In the three models shown in Fig. 2, the atmosphere must reach momentum balance with the drag applied at the bottom, which represents an interaction with an effectively infinite reservoir of momentum in the deep interior. By contrast, atmospheric angular momentum is globally conserved in the three models without drag (not shown). This important distinction could in principle have a strong impact on the atmospheric circulation regime (e.g., Rauscher & Menou 2010). We find no such major difference in our Supersol and Solar models, but there is a qualitative difference in circulation regime for the Water model without drag (not shown) relative the one with drag (top panel, Fig 2). In the drag-free model, which shows some signs of additional dynamical activity, north-south symmetry is broken. Winds in the northern hemisphere, beyond the superrotating equatorial jet, are markedly westward (negative), throughout the depth of the atmosphere. While this difference between the Water models with and without drag is clearly important, we have not explored these dynamical issues any further. Indeed, the key dynamical feature that is common to all our models is the superrotating equatorial jet, which predominantly determines the thermal signatures of GJ1214b, whether or not bottom drag is applied (see Fig. 4).

Figure 3 shows maps of outgoing thermal flux for the same three models with bottom drag as shown in Fig. 2. Since these maps are centered on the substellar point, they reveal a clearly incremental amount of eastward heat advection (and re-radiation), from the Water model (top) to the Supersol model (middle) and finally the Solar model (bottom). By

---

<sup>4</sup>Small rotational offsets from tidal-locking would yield similar results, but it is unclear what circulation regime and thermal signatures would emerge in the case of substantial deviations from tidal-locking.

contrast, heat advection towards the poles remains limited in all three models.

Figure 4 confirms these trends by showing the thermal phase curves expected for an observer located at a 90 deg inclination with respect to the planet’s rotational axis. These phase curves are calculated by integrating the flux from each visible atmospheric column at each location along the planet’s orbit, accounting for the proper geometry of emission (see Rauscher & Menou 2011b for details). Differences in the thermal phase curves of models with and without bottom drag (solid vs. dashed lines) are very small or negligible. The phase curve contrast, measured as the ratio of the maximum to minimum thermal flux, decreases from 1.9 in the Water model to 1.4 in the Supersol model and 1.09 in the Solar model. The angular offset at peak emission, relative to the time of secondary eclipse at phase 0.5, is of order 50 deg in the Water and Supersol models, and 100 deg in the Solar model. Adopting the thermal flux at phase 0.5 as a measure of secondary eclipse depth, we deduce an eclipsed flux of order  $7000 \text{ W m}^{-2}$  for the Water model,  $6200 \text{ W m}^{-2}$  for the Supersol model and  $5650 \text{ W m}^{-2}$  for the Solar model. Even for the Solar model with strong zonal transport, the eclipsed flux is above the  $5375 \text{ W m}^{-2}$  expected for perfect heat redistribution, because the polar regions remain cooler than the equator (see Fig. 3).

The differences in thermal curves shown in Fig. 4 can easily be understood as resulting from molecular weight and opacity effects. In all our model, the timescales to advect heat away from the substellar point and around the planet’s equator at the thermal photosphere are comparable, with  $\tau_{\text{adv}} \sim R_p/U$  and wind velocities  $U \sim 1\text{-}2 \text{ km/s}$  at the thermal photosphere. By contrast, radiative times at the thermal photosphere vary substantially from one model to the next. Since  $\tau_{\text{rad}} \sim C_p P / (g\sigma T^3)$ , we estimate that  $\tau_{\text{rad}}$  is about 5.5 times longer in the Supersol model than in the Water model, in proportion to their mean molecular weights (or gas constants,  $\mathcal{R}$ ). The difference in mean molecular weights between the Supersol and Solar models is a modest factor  $\sim 1.5$ , but the significantly weaker opacities in the Solar model have a large effect on the location of the thermal photosphere. A factor 5 reduction in opacities results in a thermal photosphere at 5 times greater pressure in the Solar model. Factoring both opacity and molecular weight effects, this implies that  $\tau_{\text{rad}}$  is approximately 7.5 times longer in the Solar model than it is in the Supersolar one. The substantial decrease of the ratio  $\tau_{\text{adv}}/\tau_{\text{rad}}$  in the models shown in Figs. 3 and 4, from top to bottom, combined with the prevalence of superrotating equatorial jets in all models, leads to an increasing amount of eastward heat advection (e.g. Cowan & Agol 2011; Menou 2011), which is largely responsible for the differences in phase curves shown in Fig. 4.

#### 4. Conclusion

Our results for GJ1214b are interesting in and of themselves because there is significant observational potential for obtaining robust constraints on the thermal properties of this particular exoplanet. Of course, our models of the atmospheric circulation on GJ1214b, with simple grey radiative transfer and bottom drag treatment, remain idealized. Various additional considerations could complicate our attempts to understand the regime of circulation on GJ1214b, such as the presence of clouds/hazes in the atmosphere (Miller-Ricci et al. 2011) or the possibility that the planet maintains a finite eccentricity (Charbonneau et al. 2009). This can be addressed by building models of increasing complexity as more observational constraints become available.

Although applied specifically to GJ1214b, our main arguments are simple enough that they may retain validity for other similar tidally-locked mini-Neptunes/waterworlds, such as HD97658b (Henry et al. 2011) and perhaps Kepler-11b and 11c (Lissauer et al. 2011). To the extent that superrotating equatorial jets are robust features of the atmospheric circulation regime on such planets, as suggested by our results and recent work on hot Jupiters (Showman & Polvani 2011) and hot Neptunes (Lewis et al. 2010), one can expect differences in mean-molecular weight and opacities to result in distinct thermal signatures of a similar character as the ones shown in our Fig. 3 and 4. Such considerations, combined with planet-specific atmospheric models like the ones presented here, should help us constrain the atmospheric composition of tidally-locked mini-Neptunes/waterworlds.

The author thanks Emily Rauscher for providing some of the routines used in this study. This work was supported in part by NASA grant PATM NNX11AD65G.

#### REFERENCES

- Adams, E. R., Seager, S., & Elkins-Tanton, L. 2008, *ApJ*, 673, 1160
- Bean, J. L., Miller-Ricci Kempton, E., & Homeier, D. 2010, *Nature*, 468, 669
- Bean, J. L. et al. 2011, *ApJ* submitted, arXiv:1109.0582
- Charbonneau, D., et al. 2009, *Nature*, 462, 891
- Cowan, N. B. & Agol, E. 2011, *ApJ* 729, 54
- Croll, B., Albert, L., Jayawardhana, R., Miller-Ricci Kempton, E., Fortney, J. J., Murray, N., & Neilson, H. 2011, *ApJ*, 736, 78
- Crossfield, I. J. M., Barman, T., & Hansen, B. M. S. 2011, *ApJ*, 736, 132



- Desert, J.-M., et al. 2011, *ApJ*, 731, L40+
- Guillot, T. 2010, *A&A* 520, A27
- Henry, G. W. et al. 2011, *ApJ* submitted, arXiv:1109.2549
- Hoskins, B. J. & Simmons, A. J. 1975, *Quart. J. Roy. Meteo. Soc.*, 101, 637
- Forster, de F. P. M., Blackburn, M., Glover, R. & Shine, K. P. 2000, *Climate Dynamics* 16, 833
- Fortney, J. J., Marley, M. S. & Barnes, J. W. 2007, *ApJ* 659, 1661
- Lewis, N. K. et al. 2010, *ApJ* 720, 344
- Lissauer, J. J. et al. 2011, *Nature* 470, 53
- Liu, J., Goldreich, P. M., Stevenson, D. J. 2008, *Icar.*, 653, 664
- Menou K. 2011, *ApJ* submitted, arXiv:1108.3592
- Menou, K. & Rauscher, E. 2009, *ApJ* 700, 887
- Miller-Ricci, E., Seager, S., & Sasselov, D. 2009, *ApJ*, 690, 1056
- Miller-Ricci, E. & Fortney, J. J. 2010, *ApJ* 716, L74
- Miller-Ricci Kempton, E., Zahnle, K. & Fortney, J. J. 2011, arXiv:1104.5477
- Nettelmann, N., Fortney, J. J., Kramm, U., & Redmer, R. 2011, *ApJ*, 733, 2
- Perna, R., Menou, K. & Rauscher, E., 2010, *ApJ* 719, 1421
- Rauscher, E. & Menou, K. 2010, *ApJ* 714, 1334
- Rauscher, E. & Menou, K. 2011a, *ApJ* submitted, arXiv:1105.2321
- Rauscher, E. & Menou, K. 2011b, to be submitted to *ApJ*
- Rogers, L. A. & Seager, S. 2010, *ApJ* 716, 1208
- Schneider, T. & Liu, J. 2009, *Journal of Atmospheric Sciences*, 66, 579
- Showman, A. P., Y-K. Cho, J., Menou, K. 2010, in “Exoplanets”, *Space Science Series of the University of Arizona Press* (Tucson, AZ); Ed. S. Seager; arXiv:0911.3170.
- Showman, A. P. & Polvani, L. M. 2011, *ApJ* 738, 71
- Thrustarson, H. T. & Cho, J. Y-K. 2011, *ApJ* 729, 117

Table 1. Model Parameters

Parameters	Water	Model SuperSol	Solar
$g$ (gravitational acceleration [m s <sup>-2</sup> ])	8.93	8.93	8.93
$\Omega_p$ (planetary rotation rate [rad s <sup>-1</sup> ])	$4.615 \times 10^{-5}$	$4.615 \times 10^{-5}$	$4.615 \times 10^{-5}$
$R_p$ (planetary radius [m])	$1.7 \times 10^7$	$1.7 \times 10^7$	$1.7 \times 10^7$
$\mathcal{R}$ (perfect gas constant [MKS])	483	2519	3779
$\kappa$ ( $= \mathcal{R}/c_p$ )	0.286	0.286	0.286
$k_{\text{th}}$ (thermal opacity coeff. [cm <sup>2</sup> g <sup>-1</sup> ])	0.1	0.1	$2 \times 10^{-2}$
$k_{\text{vis}}$ (visible opacity coeff. [cm <sup>2</sup> g <sup>-1</sup> ])	$4 \times 10^{-3}$	$4 \times 10^{-3}$	$8 \times 10^{-4}$

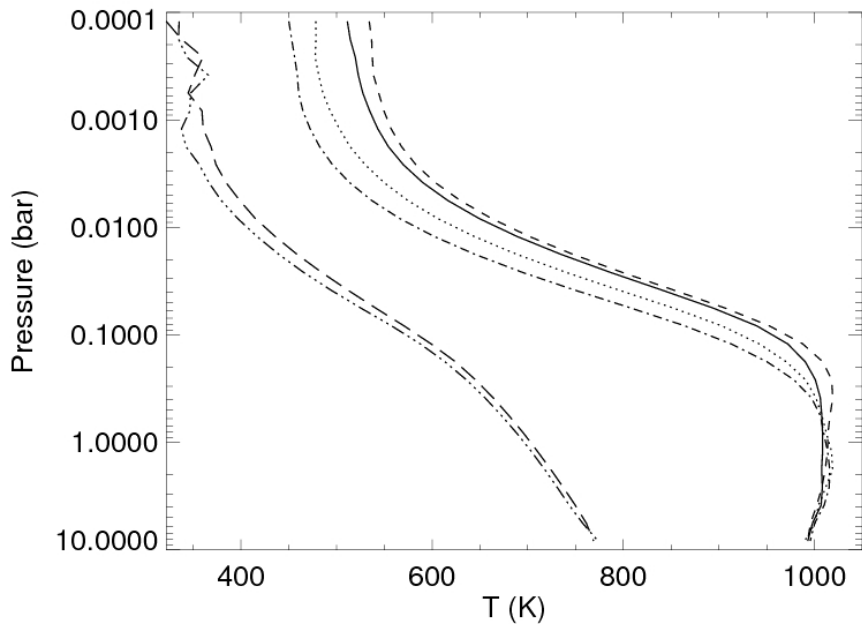


Fig. 1.— Examples of temperature-pressure profiles in the Water model with bottom drag, at six different locations around the planet (substellar point = solid line, antistellar point = dotted line, equator at east terminator = dashed line, equator at west terminator = dot-dashed line, north pole = triple dot-dashed line, south pole = long dashed line). Polar regions are significantly colder than the equatorial regions. The thick solid line shows the dayside-averaged profile obtained from Guillot’s (2010) radiative solution for identical opacities. The use of 1D averaged models to describe the transmission spectroscopic signatures of GJ1214b may be limiting, in view of the diversity of upper-atmospheric profiles found at the planetary limb in our 3D models.

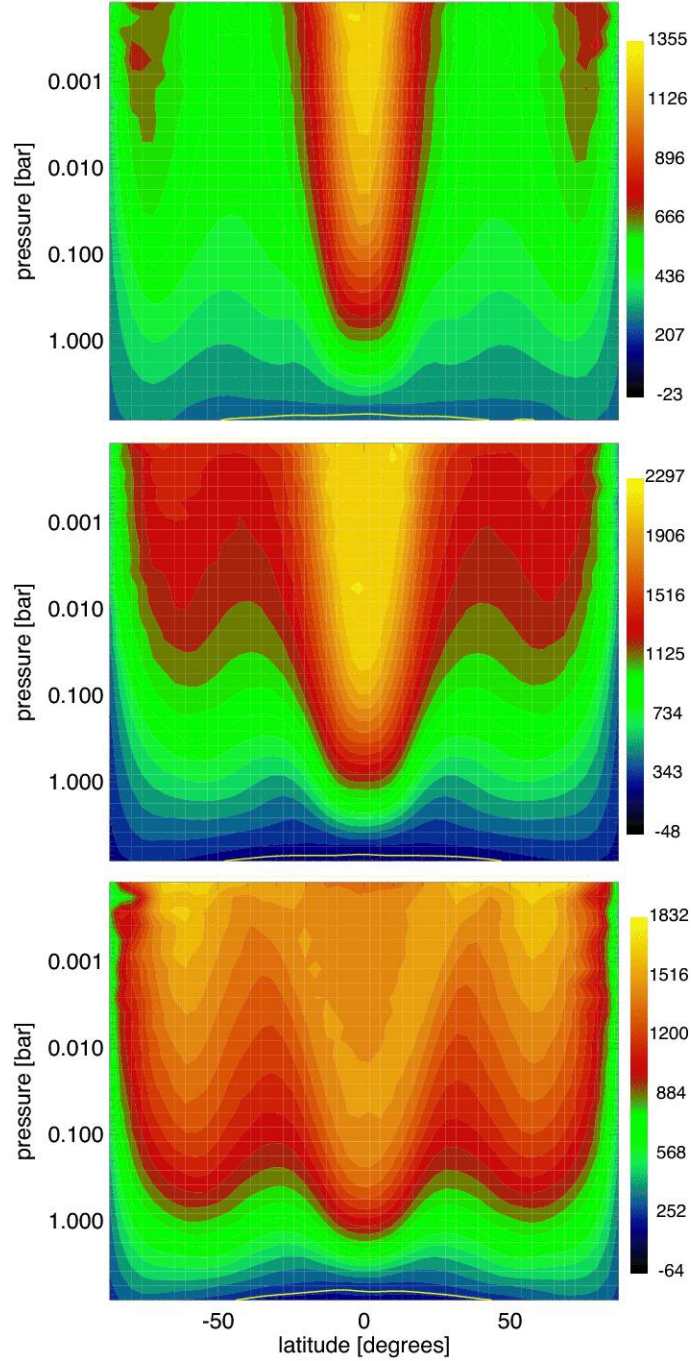


Fig. 2.— Zonal average of the zonal wind (in  $\text{m s}^{-1}$ ), as a function of latitude and pressure in the atmosphere, for the three models with bottom drag (top: Water; middle: SuperSol; bottom: Solar). A yellow line separates the regions of positive (eastward) flow and negative (westward) flow. A prominent super-rotating equatorial jet with velocities  $\sim 1\text{-}2 \text{ km s}^{-1}$  and a transition layer where bottom drag is applied are common features of all three models.

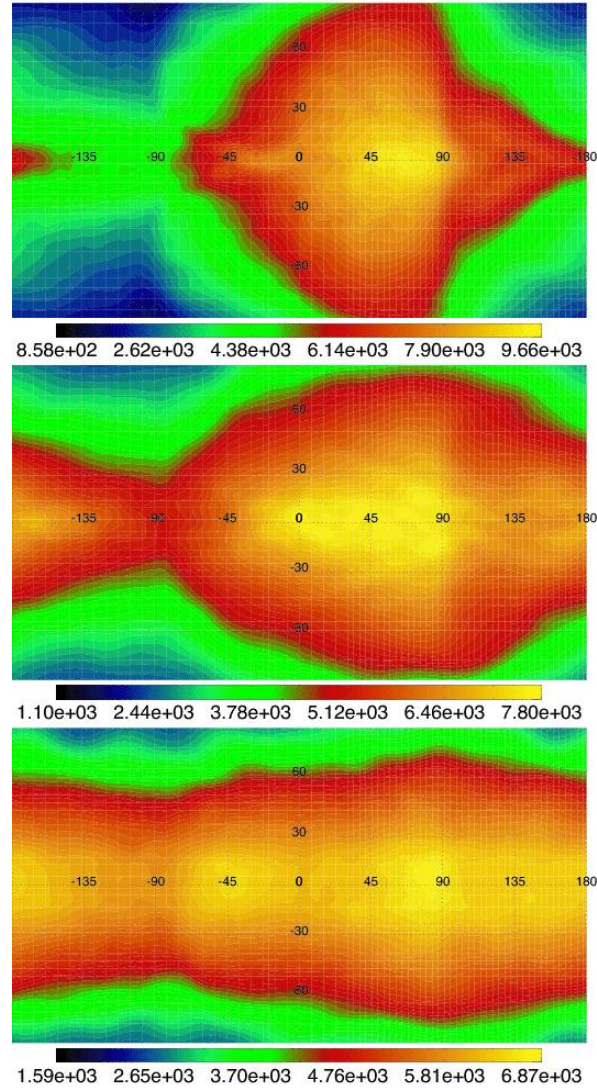


Fig. 3.— Cylindrical maps of the emerging thermal flux in the three models with bottom drag (top: Water; middle: SuperSol; bottom: Solar). Each map is centered on the substellar point and color-coded fluxes are shown in units of  $\text{W m}^{-2}$ . The degree of eastward equatorial heat transport increases significantly from the top to the bottom.

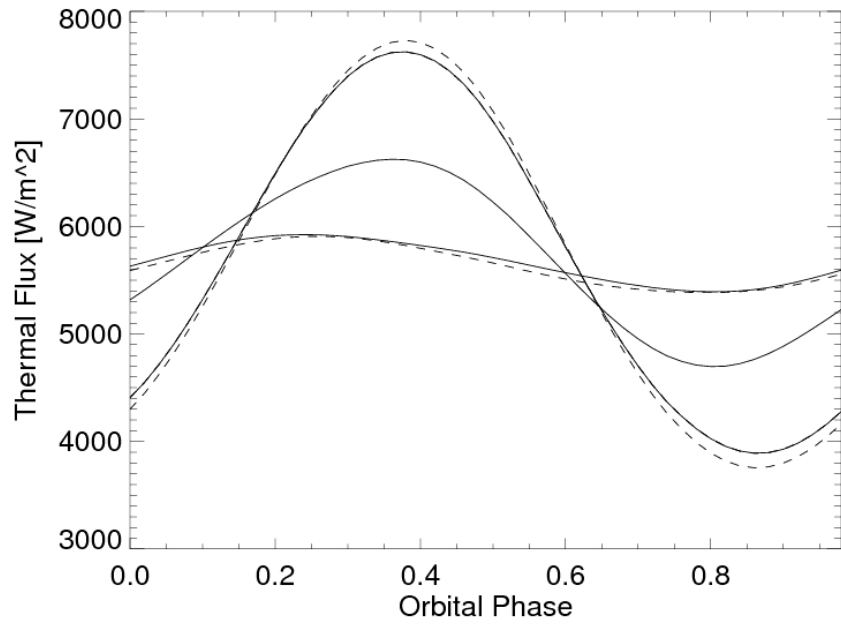


Fig. 4.— Thermal phase curves of the Water (top, at phase 0.4), Supersol (middle) and Solar (bottom) models, as seen by a distant observer in the planet’s equatorial plane. For each model, phase curves are shown in two versions, one with bottom drag (solid line) and one without it (dashed line). Transit is at orbital phase 0 and secondary eclipse is at orbital phase 0.5. Phase curve amplitudes and secondary eclipse depths are systematically reduced from the Water, to the SuperSol and finally the Solar model.